

PAPER

View Article Online
View Journal | View IssueCite this: *Energy Environ. Sci.*,
2023, 16, 5136

New insights into aliovalent substituted halide solid electrolytes for cobalt-free all-solid state batteries†

Changhong Wang,^{id} ‡^{abc} Shuo Wang,[‡] Xudong Liu,^a Yanlong Wu,^e Ruizhi Yu,^a Hui Duan,^a Jung Tae Kim,^{id} ^a Huan Huang,^c Jiantao Wang,^{*ce} Yifei Mo^{id} ^{*d} and Xueliang Sun^{id} ^{*ab}

Halide solid electrolytes (SEs) have garnered significant attention due to their decent ionic conductivity and exceptional high-voltage stability. However, their structure–property relationship remains enigmatic. In this work, we synthesize a range of $\text{Li}_{3-x}\text{Lu}_{1-x}\text{Zr}_x\text{Cl}_6$ (LLZC, $0 < x < 1$) solid solutions to investigate the influence of lithium ion and vacant site contents on ionic conductivity. Contrary to our previous understanding, it is found that achieving a balance in lithium ion and vacant site content, rather than aliovalent substitution-induced structural changes that introduce stacking faults, plays a crucial role in optimizing ion transport in a hexagonal close packing (hcp) anion framework. This balance culminates in the highest ionic conductivity (1.5 mS cm^{-1}) and lowest activation energy (0.285 eV) of LLZC. In addition, aliovalent substitution strengthens the oxidative stability of halide SSEs but reduces their reduction stability. Using LLZC as SEs and LiMn_2O_4 as cathodes, cobalt-free all-solid-state batteries undergo 1000 cycles of stable cycling at 0.3 C with negligible capacity decay.

Received 8th April 2023,
Accepted 21st August 2023

DOI: 10.1039/d3ee01119d

rsc.li/ees

Broader context

With the increasing demand for clean and sustainable energy, developing high-performance and safe energy storage has become a critical research priority. Halide solid state electrolytes (SSEs) have emerged as a promising alternative to conventional liquid electrolytes due to their high ionic conductivity and exceptional stability at high voltages. Integrating these materials into all-solid state batteries (ASSBs), which are free of liquid components and can offer higher energy density, safety, and longer cycle life, could significantly improve battery technology's performance and safety. However, the fundamental understanding of the structure–property relationship in halide SSEs is still lacking. This study highlights the design principles for developing efficient and stable halide SSEs for ASSBs. By exploring the influence of ion and vacant site concentrations on ionic conductivity, the authors found that achieving a balance in the ion and vacant site concentrations in the hexagonal close-packing anion sublattice is crucial for efficient ion transport, which leads to the highest ionic diffusivity and lowest activation energy. This study also reveals that aliovalent substitution can strengthen the oxidative stability of halide SSEs but compromise their reduction stability. This research provides important insights into developing cobalt-free ASSBs with long cycling stability, which are crucial for the widespread adoption of sustainable energy storage.

Introduction

Lithium-ion batteries (LIBs) are indispensable power sources for portable electronics, electric vehicles, and grid-scale energy storage. However, commercial LIBs contain a highly flammable liquid electrolyte, which leads to significant safety hazards, particularly in large-scale batteries. Furthermore, the energy density of commercialized LIBs will soon reach their physiochemical limit,¹ making it essential to develop next-generation energy storage technology with high energy density and improved safety. All-solid-state batteries (ASSBs) have recently gained renewed interest because of their intrinsic safety and theoretically high energy density.^{1–4} To enable ASSB technology, the primary

^a Department of Mechanical and Materials Engineering, University of Western Ontario, 1151 Richmond St, London, Ontario, N6A 3K7, Canada.
E-mail: xsun9@uwo.ca

^b Eastern Institute for Advanced Study, Eastern Institute of Technology, Ningbo, Zhejiang 3150200, P. R. China

^c Glabat Solid-State Battery Inc., 700 Collip Circle, London, ON, N6G 4X8, Canada

^d Department of Materials Science and Engineering, University of Maryland, College Park, MD, 20742, USA. E-mail: yfmo@umd.edu

^e China Automotive Battery Research Institute Co. Ltd., Beijing, P.C.101407, China.
E-mail: wangjt@glabat.com

† Electronic supplementary information (ESI) available. See DOI: <https://doi.org/10.1039/d3ee01119d>

‡ These authors contributed equally to this work.

task is designing superionic conductors (aka., solid electrolytes (SEs)) that exhibit fast ion transport behavior at room temperature. When designing SEs, several fundamental criteria should be fulfilled:⁵ (i) a stable anion framework with a high structural tolerance and weak interaction with mobile ions; (ii) a continuous ion-conduction pathway built with related vacancies and interstitial defects; and (iii) low migration energy barriers for ion hopping. Following these criteria, different anion frameworks (*i.e.*, S^{2-} , O^{2-} , BH_4^- , X^- ($X = F, Cl, Br, I$)) have been exploited to design SEs with high room-temperature ionic conductivity, representatively sulfide electrolytes (*i.e.*, $Li_{10}GeP_2S_{12}$ (12 mS cm^{-1})⁶ and $Li_{9.54}Si_{1.74}P_{1.44}S_{11.7}Cl_{0.3}$ (25 mS cm^{-1})),⁷ oxide electrolytes (*i.e.*, $Li_7La_3Zr_2O_{12}$ ⁸ and $Li_{1.4}Al_{0.4}Ti_{1.6}(PO_4)_3$),⁹ borohydrides (*i.e.*, $LiBH_4 \cdot Li$)^{10,11}, and halide electrolytes (*i.e.*, Li_3YCl_6 and Li_3YBr_6).^{12,13} Some SEs have already demonstrated ionic conductivities comparable to those of liquid electrolytes.^{6,7}

Of all the anion chemistries, monovalent halogen anions have attracted considerable research interest due to their unique physicochemical characteristics, including large ionic radii, long ionic bonds, high polarizability, weak interactions with Li-ions, and high electrochemical oxidation stability.¹⁴ Inspired by these features, many halide electrolytes based on halogen anion chemistry have been developed, such as

$\beta\text{-Li}_3\text{AlF}_6$,¹⁵ Li_3InCl_6 ,^{16,17} Li_2ZrCl_6 ,¹⁸ Li_3ScCl_6 ,¹⁹ $SmCl_3 \cdot 0.5LiCl$,²⁰ Li_3TiCl_6 ,²¹ Li_3HoBr_6 ,²² and Li_3LaI_6 .²³ In these electrolytes, ion transport occurs *via* Li-ion hopping to vacant sites in the crystal structure.²⁴ Increasing the number of vacant sites through aliovalent substitution is an effective method for enhancing ionic conductivity.²⁵ However, the correlation between the Li-ion and vacant-site concentrations and their influence on overall ionic conductivity in halide electrolytes remains unclear.

In this work, we precisely tune the chemical composition and crystal structure of $Li_{3-x}Lu_{1-x}Zr_xCl_6$ ($0 < x < 1$) solid solutions *via* aliovalent zirconium (Zr) substitution and disentangle the influence of Li-ion contents and vacant-site contents on their ionic conductivity. Contrary to our previous understanding, the balance between Li-ion and its vacant-site contents in the anion sublattice rather than aliovalent substitution-induced structural change accounts for the improved ionic conductivity, especially in the hexagonal close packing (hcp) anion framework, because the structural change brings in stacking faults that hinder ion transport along the *c*-direction. Following this mechanism, $Li_{2.5}Lu_{0.5}Zr_{0.5}Cl_6$ presents the highest ionic conductivity and lowest activation energy when the Li-ion content is equal to the vacant site content. Furthermore, aliovalent substitution strengthens the oxidative stability of

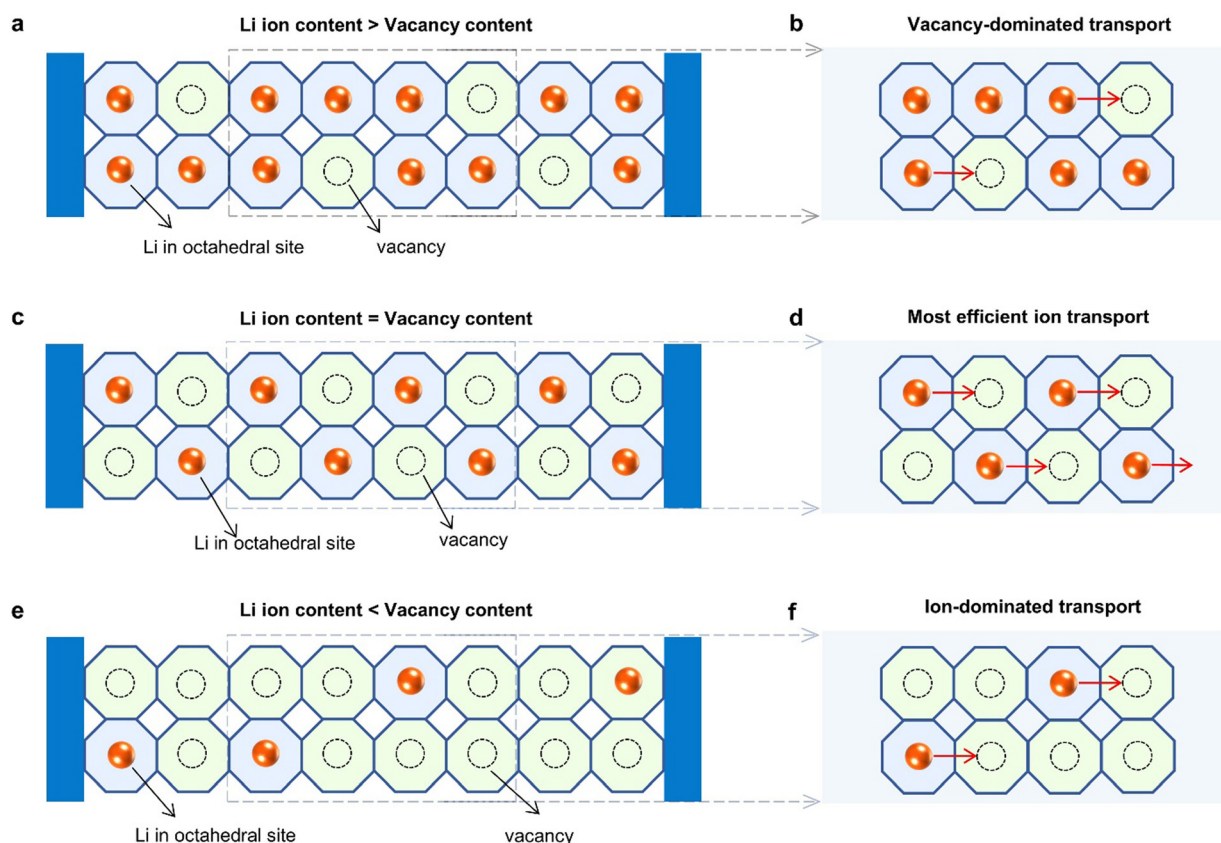


Fig. 1 Different transport scenarios contingent on ion and vacant site concentrations. (a) and (b) When the ion content is greater than the vacant site content in the sublattice, it shows vacancy-dominated transport. (c) and (d) When the ion content is equal to the vacant site content in the sublattice, it possesses the most efficient ion transport. (e) and (f) When the ion content is lower than the vacant site content, it follows an ion-dominated transport mechanism. Thus, the low ion concentration leads to low ionic conductivity.

halide SEs but compromises their reduction stability. Using $\text{Li}_{2.5}\text{Lu}_{0.5}\text{Zr}_{0.5}\text{Cl}_6$ as the SE, cobalt-free LiMn_2O_4 -based all-solid-state batteries demonstrate stable cycling over 1000 cycles at 0.3 C with negligible capacity fading. The mechanistic insights gained from this study will be of assistance in designing a solid-state halide electrolyte with the highest ionic conductivity and safer and more sustainable energy storage systems employing it.

Results and discussion

In halide SEs with a general formula of Li_3MX_6 (M = trivalent cations and X = halogen anions), cations always occupy octahedral sites coordinated by six halogen anions *via* ionic bonding.¹⁹ All the Li-ions diffuse through a three-dimensional conduction network consisting of face-sharing or tetrahedron-connected octahedra.²⁴ The ion diffusion in the halogen anion framework follows the ion hopping mechanism *via* vacancies.²⁶ To disentangle the effect of ion and vacant site concentrations on the ionic conductivity of halide SEs, we purposely designed three scenarios with different ion and vacant site concentrations in the same anion framework (Fig. 1): (1) when the Li-ion content is greater than the vacant site content in the chloride framework, the available vacant site for Li-ion hopping is limited. Thus, the ionic conductivity is limited by the low vacant site concentration (Fig. 1a and b). (2) When the Li-ion content is less than the

vacant site content, the mobile Li-ions available for ion transport are then limited. Thus, the ionic conductivity is limited by low mobile Li-ion concentrations (Fig. 1e and f). (3) When the Li-ion content is equal to the vacant site content, ion transport is most efficient, thus showing optimal ionic conductivity (Fig. 1c and d). For this purpose, $\text{Li}_{3-x}\text{Lu}_{1-x}\text{Zr}_x\text{Cl}_6$ ($0 < x < 1$) solid solutions are selected as the representative halide electrolytes because both Li_3LuCl_6 and Zr-doped Li_3LuCl_6 have *pnma* structures (Table S1, ESI†). The structural likeness minimizes the interference of other factors (*i.e.*, structural change, ion-transport pathway change, and cation disorder) as much as possible when investigating the effect of ion and vacant site concentrations on the ionic conductivity of halide SEs.

Structural analysis of Li–Lu–Zr–Cl solid solutions

High-resolution X-ray diffraction (XRD) was performed to understand the structure change of Zr substitution in the Li_3LuCl_6 matrix. The high-resolution pattern was refined (Fig. S1, ESI†), and the detailed structural information is listed in Table S2–S5 (ESI†). The linear relationship between the unit cell volume and lattice parameters in the range from 0.25 to 0.75 indicates the formation of Li–Lu–Zr–Cl solid solutions (Fig. S2, ESI†). The Li_3LuCl_6 matrix has an orthorhombic framework with a *pnma* space group (Fig. 2a), which is different from previous works using a matrix (*e.g.*, Li_3YCl_6 , Li_3ErCl_6 , and Li_3YbCl_6) with a

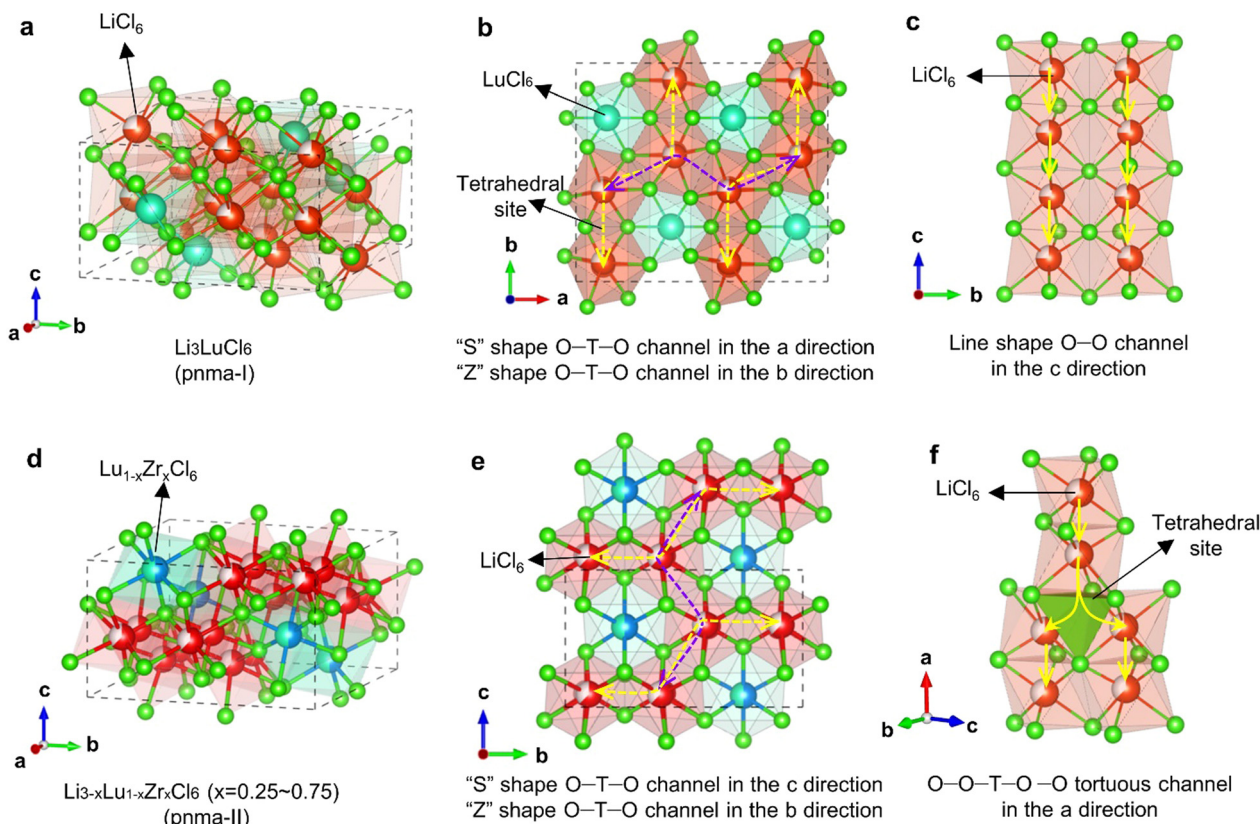


Fig. 2 Structural analysis of Li–Lu–Zr–Cl solid solutions. (a) Crystal structure of Li_3LuCl_6 . (b) Ion conduction pathways in *a* and *b* directions. (c) Ion conduction pathway in the *c* direction. (d) Crystal structure of $\text{Li}_{3-x}\text{Lu}_{1-x}\text{Zr}_x\text{Cl}_6$ ($x = 0.25\text{--}0.75$). (e) Ion conduction pathways in *b* and *c* directions. (f) Ion conduction pathway in the *a* direction.

trigonal structure (space group $P\bar{3}m1$).^{27–29} With Zr-doping, $\text{Li}_{3-x}\text{Lu}_{1-x}\text{Zr}_x\text{Cl}_6$ ($0.25 \leq x \leq 0.75$) solid solutions still maintained the orthorhombic framework with the space group ($pnma$) (Fig. 2d). However, MCl_6 octahedra became tilted, and the cations rearranged (Fig. S3, ESI†), as confirmed by $g(r)$ analysis (Fig. S4, ESI†).

Due to the cation rearrangement, the ion transport pathways also changed in the $\text{Li}_{3-x}\text{Lu}_{1-x}\text{Zr}_x\text{Cl}_6$ solid solutions. As shown in Fig. 2b, Li_3LuCl_6 with the $pnma$ -I structure has an “S” shape of octa-tetra-octa (O–T–O) conduction pathways in the a direction and a “Z” shape of O–T–O conduction pathways in the b direction. In the c direction, Li_3LuCl_6 possesses linear octa-to-octa (O–O) conduction pathways (Fig. 2c). Comparatively, $\text{Li}_{3-x}\text{Lu}_{1-x}\text{Zr}_x\text{Cl}_6$ solid solutions with the $pnma$ -II structure have an “S” shape of the O–T–O ion pathway in the c direction and a “Z” shape of the O–T–O conduction pathway in the b direction (Fig. 2e). However, $\text{Li}_{3-x}\text{Lu}_{1-x}\text{Zr}_x\text{Cl}_6$ has a tortuous O–O–T–O–T conduction pathway in a direction as stacking faults are introduced (Fig. 2f).¹³ Based on previous theoretical calculations,²⁴ the O–T–O conduction channel possesses a higher energy barrier than the O–O conduction channels in the anion sublattice. Therefore, this structural change cannot explain the ionic conductivity improvements,

as demonstrated in previous ref. 27 and 28. Moreover, the cation-blocking effect should be more prominent in the Li–Lu–Zr–Cl solid solutions because tetravalent Zr^{4+} has a more significant coulombic repulsive force than trivalent Lu^{3+} , which prevents Li-ion transport *via* the tetrahedral site around MCl_6 octahedra.^{14,25} Therefore, the structural change from $pnma$ -I to $pnma$ -II cannot fully explain the improved ionic conductivity of Zr-doped Li_3MCl_6 solid solutions. Other decisive factors, such as the lithium-ion and vacant site concentrations in the structure, should also be considered and carefully investigated because they intrinsically affect the ionic conductivity in accordance with the Arrhenius–Einstein equation.

Effect of vacant site concentrations in the hcp anion sublattice

High-resolution XRD results confirm that Li–Lu–Zr–Cl solid solutions do not undergo a structural change when Zr substitution increases from 0.25 to 0.75 (Fig. S5, ESI†). In addition, the radial distribution function $g(r)$ of the framework sublattices without mobile ions remains the same at different Zr substitutions (Fig. 3a), confirming that the crystal structure remains the same.

Through aliovalent zirconium substitution (Zr^{4+} , 72 pm) with Lu, the Li-ion content in the chloride sublattice can be

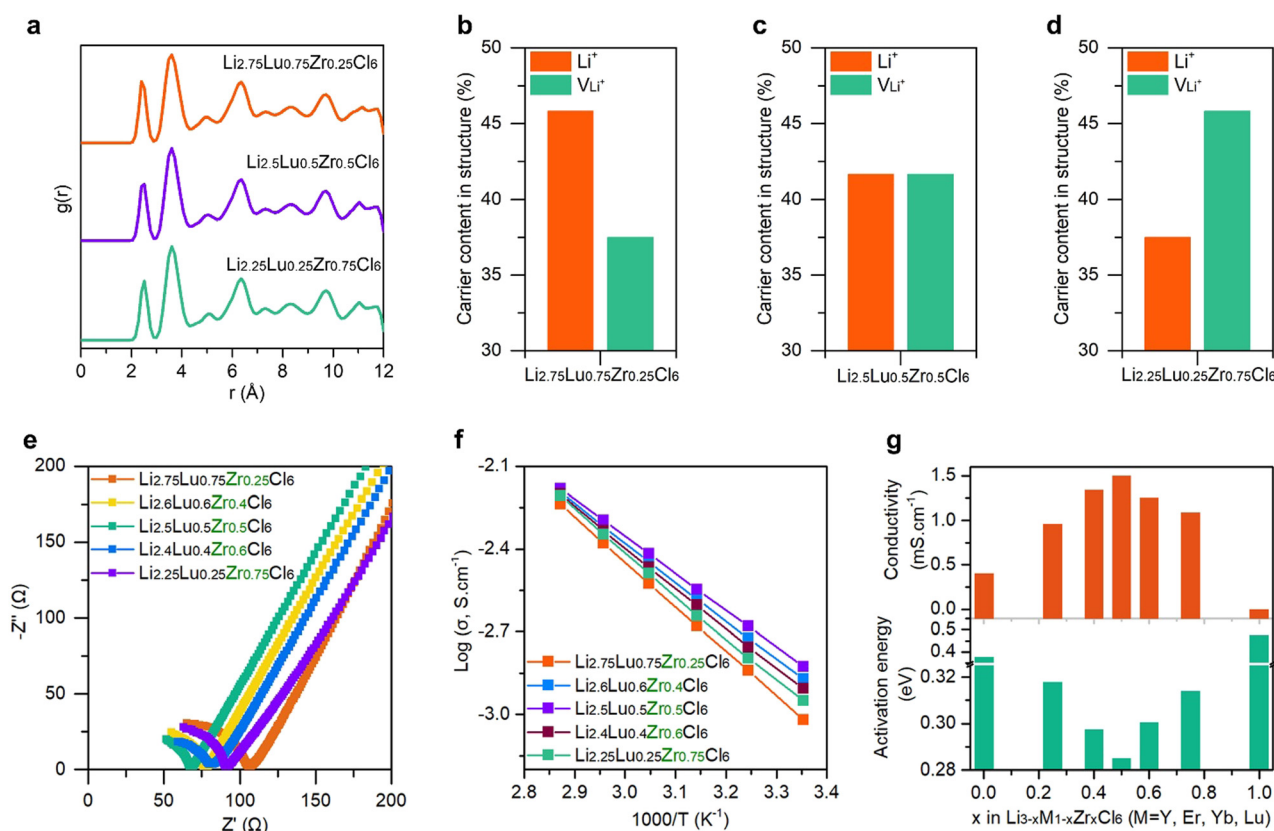


Fig. 3 Tailoring Li-ion and vacant site contents in $\text{Li}_{3-x}\text{Lu}_{1-x}\text{Zr}_x\text{Cl}_6$ (LLZC) solid solutions and their electrochemical properties. (a) The radial distribution function $g(r)$ of the $pnma$ -II sublattice without mobile ions at different Zr substitutions. The relationship of lithium-ion and vacant site contents in halide electrolytes: (b) $\text{Li}_{2.75}\text{Lu}_{0.75}\text{Zr}_{0.25}\text{Cl}_6$, (c) $\text{Li}_{2.5}\text{Lu}_{0.5}\text{Zr}_{0.5}\text{Cl}_6$, and (d) $\text{Li}_{2.25}\text{Lu}_{0.75}\text{Zr}_{0.25}\text{Cl}_6$. (e) EIS profile of LLZC solid solutions at room temperature. (f) Arrhenius plot of LLZC solid solutions. (g) The relationship between the chemical composition of LLZC and corresponding room-temperature ionic conductivity and activation energy.

decreased while the vacant site content can be increased (Fig. S6, ESI†). When 25% of Zr^{4+} substitutes Lu^{3+} , the vacant site content increases to 37.5% (Fig. 3b). When half of Lu^{3+} is substituted by Zr^{4+} , the Li-ion concentration and the vacant-site content are balanced (Fig. 3c). Further aliovalent substitution reverses the relationship between the Li-ion and the vacant site (Fig. 3d). Fig. 3e shows the electrochemical impedance spectroscopy (EIS) profiles of the Li–Lu–Zr–Cl solid solutions at room temperature (RT). The ionic conductivity of Li_3LuCl_6 at RT is 0.40 mS cm^{-1} . With 25% Zr substitution, the ionic conductivity increases to 0.96 mS cm^{-1} . With 50% Zr substitution, the ionic conductivity increases to 1.50 mS cm^{-1} with a low electronic conductivity of $6.75 \times 10^{-10} \text{ S cm}^{-1}$ (Fig. S7, ESI†). Further increasing the Zr content to 75% lowers the ionic conductivity to 1.12 mS cm^{-1} . To determine the activation energy, temperature-dependent EIS was measured and is displayed in Fig. S8 (ESI†). Fig. 2f presents the Arrhenius plots of $\text{Li}_{3-x}\text{Lu}_{1-x}\text{Zr}_x\text{Cl}_6$ ($x = 0, 0.25, 0.5, 0.75$) solid solutions. The room temperature ionic conductivity and corresponding activation energy are plotted in Fig. 3g. Indeed, $\text{Li}_{2.5}\text{Lu}_{0.5}\text{Zr}_{0.5}\text{Cl}_6$ exhibits the highest ionic conductivity (1.50 mS cm^{-1}) and the lowest activation energy (0.285 eV), in which the Li vacant site and Li-ion contents are equivalent in the anion sublattice. Not only do our cases, but other solid solutions (e.g., Li–Y–Zr–Cl,²⁸ Li–Er–Zr–Cl,²⁸ Li–Yb–Zr–Cl,²⁷ Li–Yb–Hf–Cl,²⁹ and Li–Zr–In–Cl³⁰) also show the highest ionic conductivity when ion and vacant site contents are balanced (Fig. S9, ESI†), implying that balancing the Li-ion and vacant site contents is crucial for obtaining their optimal ionic conductivity. Moreover, we performed AMID simulations on $\text{Li}_{3-x}\text{Lu}_{1-x}\text{Zr}_x\text{Cl}_6$ ($x = 0.25, 0.5, 0.75$). The simulation results confirm that $\text{Li}_{2.5}\text{Lu}_{0.5}\text{Zr}_{0.5}\text{Cl}_6$ shows the highest Li-ion conductivity and lowest activation energy ($0.20 \pm 0.02 \text{ eV}$) compared to $\text{Li}_{2.25}\text{Lu}_{0.25}\text{Zr}_{0.75}\text{Cl}_6$ ($0.23 \pm 0.02 \text{ eV}$) and $\text{Li}_{2.75}\text{Lu}_{0.75}\text{Zr}_{0.25}\text{Cl}_6$ ($0.30 \pm 0.03 \text{ eV}$) (Fig. S10, ESI†). Both experimental results and theoretical calculations consistently demonstrate that balancing the Li-ion and vacant site concentrations plays a crucial role in obtaining the highest ionic conductivity in the hexagonal closest pack (hcp) anion sublattice.

Electrochemical windows

To gain further insights into the intrinsic electrochemical window of halide SEs, cyclic voltammetry (CV) was conducted on $\text{Li}_{2.5}\text{Lu}_{0.5}\text{Zr}_{0.5}\text{Cl}_6$ with 20% carbon, which provides sufficient electron conduction pathways (Fig. 4a).³¹ $\text{Li}_{2.5}\text{Lu}_{0.5}\text{Zr}_{0.5}\text{Cl}_6$ is exceptionally stable during oxidative scanning. Only when magnifying the CV profile do we see that $\text{Li}_{2.5}\text{Lu}_{0.5}\text{Zr}_{0.5}\text{Cl}_6$ is slightly oxidized at 4.25 V (Fig. 4b). The high oxidative stability is beneficial for the cycling stability of high-voltage ASSBs. A small shoulder peak at around 4.0 V is also observed, likely originating from some impurities of precursors (LuCl_3). Compared to Li_3LuCl_6 , aliovalent substitution (e.g., Zr^{4+} and Hf^{4+}) strengthens the oxidative stability of halide SEs at the expense of their reduction stability as two peaks at 1.75 V (vs. Li^+/Li) and 0.7 V (vs. Li^+/Li) are detected during reductive scanning. Based on the first principles calculations (Fig. 4c), the 1.75 V peak is

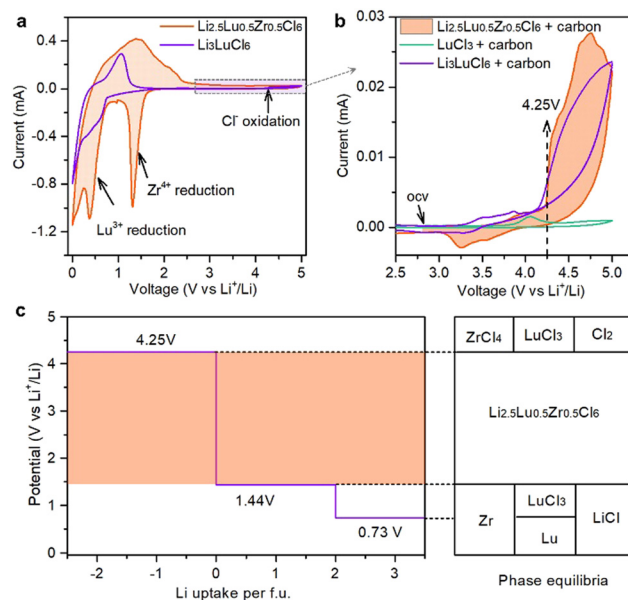


Fig. 4 Intrinsic electrochemical windows of $\text{Li}_{2.5}\text{Lu}_{0.5}\text{Zr}_{0.5}\text{Cl}_6$. (a) CV profiles of $\text{Li}_{2.5}\text{Lu}_{0.5}\text{Zr}_{0.5}\text{Cl}_6$ and Li_3LuCl_6 . (b) Enlarged region of the CV profile from the open-circuit voltage (ocv) to 5V. (c) The first-principles calculation results of the voltage profile and phase equilibria of $\text{Li}_{2.5}\text{Lu}_{0.5}\text{Zr}_{0.5}\text{Cl}_6$.

ascribed to Zr^{4+} reduction, and the 0.7 V peak is related to Lu^{3+} reduction.

Electrochemical performance of cobalt-free all-solid-state batteries

Spinel LiMn_2O_4 has been considered one of the most promising cathodes due to its high output voltage, low cost, abundance, environmental affinity, good ion diffusion kinetics, and better thermal stability compared to layered cathodes (i.e., LiCoO_2 and $\text{LiNi}_x\text{Mn}_y\text{Co}_z\text{O}_2$ ($x + y + z = 1$)) (Fig. S11, ESI†).^{32,33} Despite this, LiMn_2O_4 cathodes have received less attention than layered cathodes in the ASSB configuration. Based on our understanding, there are several advantages to developing cobalt-free LiMn_2O_4 -based ASSBs with halide electrolytes. First, LiMn_2O_4 has three-dimensional Li-ion transport channels, which is beneficial for obtaining high-rate performance in ASSBs. Second, the voltage range of LiMn_2O_4 is from 3.0 to 4.3 V, which is entirely compatible with the electrochemical stability window of $\text{Li}_{2.5}\text{Lu}_{0.5}\text{Zr}_{0.5}\text{Cl}_6$. Third, LiMn_2O_4 suffers from notorious Mn dissolution in the liquid cell, which can be completely avoided in a solid-state configuration.

For these reasons, we constructed a LiMn_2O_4 -based ASSB with the solid-state halide electrolyte $\text{Li}_{2.5}\text{Lu}_{0.5}\text{Zr}_{0.5}\text{Cl}_6$ (Fig. 5a). Fig. 5b shows an SEM image of the cross-sectional structure of LiMn_2O_4 -based ASSBs. Fig. 5c compares the initial charge–discharge curves of LiMn_2O_4 in both liquid cells and ASSBs at 0.1C ($1\text{C} = 120 \text{ mA g}^{-1}$). LiMn_2O_4 in ASSBs shows a high initial capacity of $119.4 \text{ mA h g}^{-1}$ with a high coulombic efficiency of 91.8% at 0.1C . The high utilization of LiMn_2O_4 in ASSBs indicates that LiMn_2O_4 is in good contact with $\text{Li}_{2.5}\text{Lu}_{0.5}\text{Zr}_{0.5}\text{Cl}_6$, as confirmed by the scanning electron microscopy (SEM) images

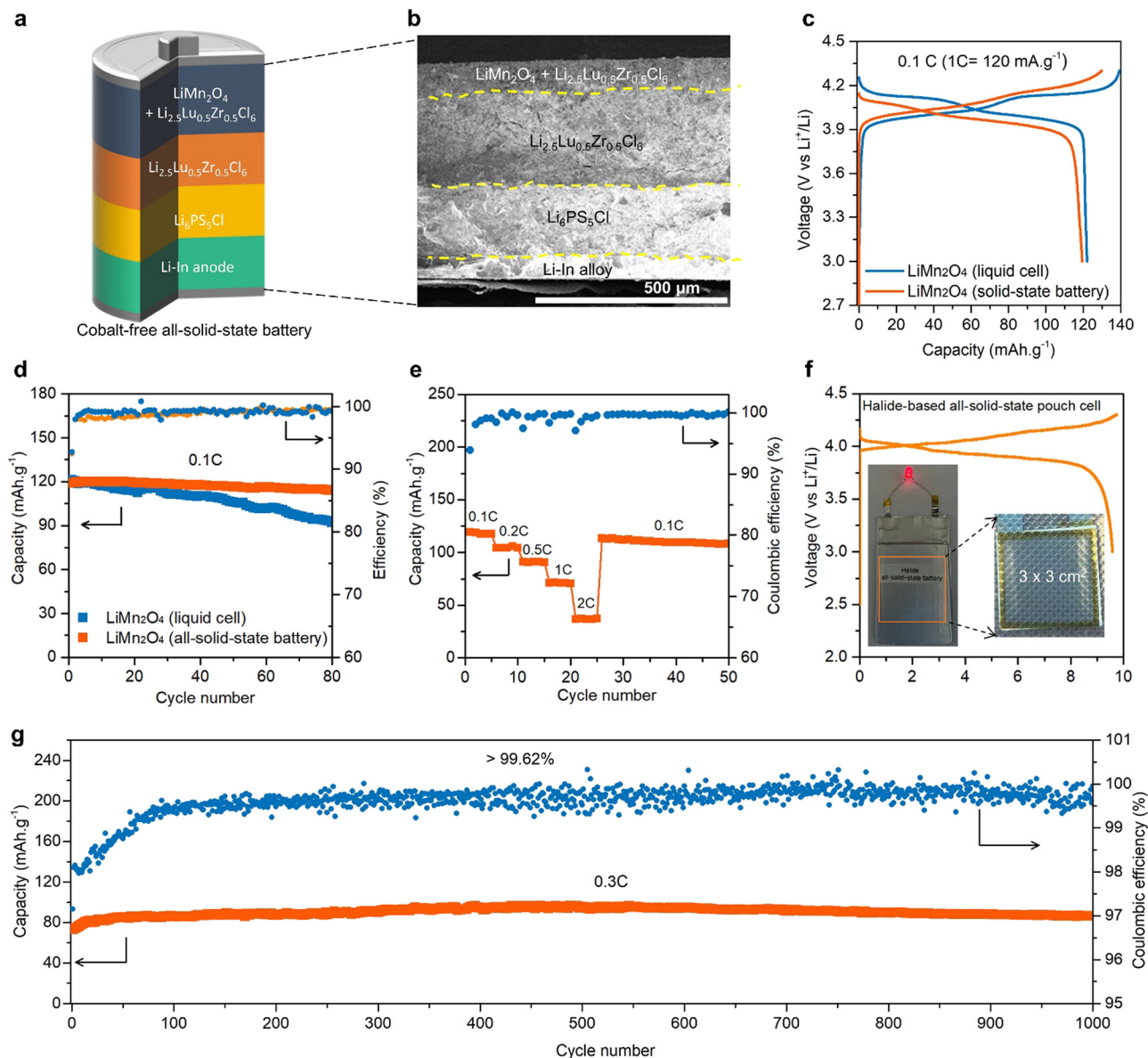


Fig. 5 Electrochemical performance of cobalt-free all-solid-state batteries with a configuration of $\text{LiMn}_2\text{O}_4/\text{LLZC}/\text{Li}_6\text{PS}_5\text{Cl}/\text{Li-In}$. (a) Schematic illustration of halide-based all-solid-state batteries using LiMn_2O_4 as the cathode. (b) SEM image of cross-sectional ASSBs. (c) Initial charge-discharge curves of LiMn_2O_4 in liquid cells in comparison with all-solid-state batteries. (d) Cycling stability at 0.1C. (e) Rate performance. (f) The charge/discharge curve of halide-based all-solid-state pouch cells with the LiMn_2O_4 cathode. The inset shows a photograph of a $3 \times 3 \text{ cm}^2$ halide-based all-solid-state pouch cell. (g) Long-term cycling stability at 0.3C with a high pressure of 150 MPa.

of cross-sectional ASSBs with their elemental mapping (Fig. S12, ESI[†]). Fig. 5d compares the cycling stability of LiMn_2O_4 in ASSBs and liquid cells. In liquid cells, the discharge capacity decays very fast, which most likely stems from the dissolution of manganese and structural changes caused by the Jahn-Teller effect.^{32,33} In contrast, LiMn_2O_4 -based ASSBs demonstrate stable cycling stability at 0.1C. The capacity retention after 80 cycles is as high as 94.2%, indicating that an ASSB configuration can avoid the issue of Mn dissolution. X-ray photoelectron spectroscopy (XPS) further confirms that Mn dissolution is prevented in ASSBs (Fig. S13, ESI[†]). Fig. 5e presents the rate performance of ASSBs, and the corresponding discharge curves are shown in Fig. S14

(ESI[†]). A specific capacity of 42 mA h g^{-1} was achieved at 2 C. The good rate performance originates from the three-dimensional lithium-ion transport channels of LiMn_2O_4 and the high ionic conductivity of $\text{Li}_{2.5}\text{Lu}_{0.5}\text{Zr}_{0.5}\text{Cl}_6$. Furthermore, a halide-based all-solid-state pouch cell with a dimension of $3 \times 3 \text{ cm}^2$ was fabricated using the dry-film process (Fig. 5f).³⁴ This all-solid-state pouch cell exhibits a capacity of 9.58 mA h, a high coulombic efficiency of 98.4%, and excellent cycling stability (Fig. S15, ESI[†]), and can successfully light on a LED bulb and power on an electric fan (Video S1, ESI[†]). To evaluate the long-term cycling stability, ASSBs were also tested at 0.3 C (Fig. 5g), which demonstrated a capacity of approximately 98 mA h g^{-1}

when cycled at 0.3 C with no capacity decay over 1000 cycles, which is attributed to the good interfacial chemical and electrochemical compatibility between $\text{Li}_{2.5}\text{Lu}_{0.5}\text{Zr}_{0.5}\text{Cl}_6$ and LiMn_2O_4 (Fig. S16, ESI†). The ascending trend in Coulombic efficiency over the initial 90 cycles (in Fig. 5g) is attributed to both the stabilization of the interface and the alleviation of internal stress resulting from the application of an large external pressure (150 MPa). These results demonstrate the first comprehensive assessment of cobalt-free and low-cost LiMn_2O_4 cathodes in ASSBs, particularly by employing solid-state halide electrolytes.

Conclusions

To summarize, we synthesized a series of $\text{Li}_{3-x}\text{Lu}_{1-x}\text{Zr}_x\text{Cl}_6$ ($0 < x < 1$) solid solutions to explore the influence of ion and vacant site concentrations on ionic conductivity. We discovered that when 50% of Lu^{3+} is substituted by Zr^{4+} , the lithium-ion and vacant-site concentrations are balanced in $\text{Li}_{3-x}\text{Lu}_{1-x}\text{Zr}_x\text{Cl}_6$ solid solutions, which leads to the highest ionic conductivity of 1.5 mS cm^{-1} at room temperature. Our findings revealed that achieving a balance in the ion and vacant site concentrations in the halogen anion sublattice, rather than inducing structural changes by aliovalent substitution, plays a crucial role in efficient ion transport, which leads to the highest ionic diffusivity and lowest activation energy. In addition, we also found that aliovalent substitution, such as Zr^{4+} or Hf^{4+} , strengthens the oxidative stability of halide SEs but compromises their reduction stability. Using LiMn_2O_4 as the cathode and $\text{Li}_{2.5}\text{Lu}_{0.5}\text{Zr}_{0.5}\text{Cl}_6$ as the SE, the cobalt-free ASSB demonstrated satisfactory electrochemical performance, particularly long cycling stability with a negligible capacity decay over 1000 cycles at 0.3C. Furthermore, a halide all-solid-state pouch cell is successfully demonstrated. This work provides a new design principle for designing solid-state halide electrolytes with optimal ionic conductivity and lays the groundwork for future research into cobalt-free all-solid-state batteries with long cycling stability.

Data availability

The data that support the findings of this study are available from the corresponding author upon reasonable request.

Author contributions

C. Wang conceived the idea, performed all the materials synthesis, conducted characterization and analysis, and wrote the manuscript. S. Wang performed the first principles calculations, analyzed the data, and wrote the manuscript. X. Liu, Y. Wu, R. Yu, and H. Duan helped with electrochemical testing. H. Huang provided chemicals. Prof. J. Wang, Prof. Y. Mo, and Prof. X. Sun supervised the whole project.

Conflicts of interest

There are no conflicts to declare.

Acknowledgements

This work was supported by the Natural Sciences and Engineering Research Council of Canada (NSERC), the Canada Research Chair Program (CRC), the Canada Foundation for Innovation (CFI), the Ontario Research Fund, and the University of Western Ontario. C. Wang acknowledges the Banting Postdoctoral Fellowship (BPF-180162).

References

- 1 J. Janek and W. G. Zeier, *Nat. Energy*, 2016, **1**, 16141.
- 2 C. Wang, J. Liang, Y. Zhao, M. Zheng, X. Li and X. Sun, *Energy Environ. Sci.*, 2021, **14**, 2577–2619.
- 3 Y.-G. Lee, S. Fujiki, C. Jung, N. Suzuki, N. Yashiro, R. Omoda, D.-S. Ko, T. Shiratsuchi, T. Sugimoto, S. Ryu, J. H. Ku, T. Watanabe, Y. Park, Y. Aihara, D. Im and I. T. Han, *Nat. Energy*, 2020, **5**, 299–308.
- 4 D. H. S. Tan, A. Banerjee, Z. Chen and Y. S. Meng, *Nat. Nanotechnol.*, 2020, **15**, 170–180.
- 5 C. Wang, J. Liang, J. T. Kim and X. Sun, *Sci. Adv.*, 2022, **8**, eadc9516.
- 6 N. Kamaya, K. Homma, Y. Yamakawa, M. Hirayama, R. Kanno, M. Yonemura, T. Kamiyama, Y. Kato, S. Hama, K. Kawamoto and A. Mitsui, *Nat. Mater.*, 2011, **10**, 682–686.
- 7 Y. Kato, S. Hori, T. Saito, K. Suzuki, M. Hirayama, A. Mitsui, M. Yonemura, H. Iba and R. Kanno, *Nat. Energy*, 2016, **1**, 16030.
- 8 R. Murugan, V. Thangadurai and W. Weppner, *Angew. Chem., Int. Ed.*, 2007, **46**, 7778–7781.
- 9 C. Wang, Q. Sun, Y. Liu, Y. Zhao, X. Li, X. Lin, M. N. Banis, M. Li, W. Li, K. R. Adair, D. Wang, J. Liang, R. Li, L. Zhang, R. Yang, S. Lu and X. Sun, *Nano Energy*, 2018, **48**, 35–43.
- 10 M. Matsuo, Y. Nakamori, S.-I. Orimo, H. Maekawa and H. Takamura, *Appl. Phys. Lett.*, 2007, **91**, 224103.
- 11 H. Maekawa, M. Matsuo, H. Takamura, M. Ando, Y. Noda, T. Karahashi and S.-I. Orimo, *J. Am. Chem. Soc.*, 2009, **131**, 894–895.
- 12 T. Asano, A. Sakai, S. Ouchi, M. Sakaida, A. Miyazaki and S. Hasegawa, *Adv. Mater.*, 2018, 1803075.
- 13 E. Sebt, H. A. Evans, H. Chen, P. M. Richardson, K. M. White, R. Giovine, K. P. Koirala, Y. Xu, E. Gonzalez-Correa, C. Wang, C. M. Brown, A. K. Cheetham, P. Canepa and R. J. Clément, *J. Am. Chem. Soc.*, 2022, **144**, 5795–5811.
- 14 J. Liang, X. Li, K. R. Adair and X. Sun, *Acc. Chem. Res.*, 2021, **54**, 1023–1033.
- 15 M. Feinauer, H. Euchner, M. Fichtner and M. A. Reddy, *ACS Appl. Energy Mater.*, 2019, **2**, 7196–7203.
- 16 X. Li, J. Liang, J. Luo, M. Norouzi Banis, C. Wang, W. Li, S. Deng, C. Yu, F. Zhao, Y. Hu, T.-K. Sham, L. Zhang, S. Zhao, S. Lu, H. Huang, R. Li, K. R. Adair and X. Sun, *Energy Environ. Sci.*, 2019, **12**, 2665–2671.

- 17 X. Li, J. Liang, N. Chen, J. Luo, K. R. Adair, C. Wang, M. N. Banis, T. K. Sham, L. Zhang and S. Zhao, *Angew. Chem., Int. Ed.*, 2019, **131**, 16579–16584.
- 18 K. Wang, Q. Ren, Z. Gu, C. Duan, J. Wang, F. Zhu, Y. Fu, J. Hao, J. Zhu, L. He, C.-W. Wang, Y. Lu, J. Ma and C. Ma, *Nat. Commun.*, 2021, **12**, 4410.
- 19 J. Liang, X. Li, S. Wang, K. R. Adair, W. Li, Y. Zhao, C. Wang, Y. Hu, L. Zhang and S. Zhao, *J. Am. Chem. Soc.*, 2020, **142**, 7012–7022.
- 20 J. Fu, S. Wang, J. Liang, S. H. Alahakoon, D. Wu, J. Luo, H. Duan, S. Zhang, F. Zhao, W. Li, M. Li, X. Hao, X. Li, J. Chen, N. Chen, G. King, L.-Y. Chang, R. Li, Y. Huang, M. Gu, T.-K. Sham, Y. Mo and X. Sun, *J. Am. Chem. Soc.*, 2023, **145**, 2183–2194.
- 21 K. Wang, Z. Gu, Z. Xi, L. Hu and C. Ma, *Nat. Commun.*, 2023, **14**, 1396.
- 22 X. Shi, Z. Zeng, M. Sun, B. Huang, H. Zhang, W. Luo, Y. Huang, Y. Du and C. Yan, *Nano Lett.*, 2021, **21**, 9325–9331.
- 23 Z. Xu, X. Chen, K. Liu, R. Chen, X. Zeng and H. Zhu, *Chem. Mater.*, 2019, **31**, 7425–7433.
- 24 S. Wang, Q. Bai, A. M. Nolan, Y. Liu, S. Gong, Q. Sun and Y. Mo, *Angew. Chem., Int. Ed.*, 2019, **58**, 8039–8043.
- 25 Y. Liu, S. Wang, A. M. Nolan, C. Ling and Y. Mo, *Adv. Energy Mater.*, 2020, **10**, 2002356.
- 26 Y. Gao, A. M. Nolan, P. Du, Y. Wu, C. Yang, Q. Chen, Y. Mo and S.-H. Bo, *Chem. Rev.*, 2020, **120**, 5954–6008.
- 27 S. Y. Kim, K. Kaup, K.-H. Park, A. Assoud, L. Zhou, J. Liu, X. Wu and L. F. Nazar, *ACS Mater. Lett.*, 2021, **3**, 930–938.
- 28 K.-H. Park, K. Kaup, A. Assoud, Q. Zhang, X. Wu and L. F. Nazar, *ACS Energy Lett.*, 2020, **5**, 533–539.
- 29 J. Park, D. Han, H. Kwak, Y. Han, Y. J. Choi, K.-W. Nam and Y. S. Jung, *Chem. Eng. J.*, 2021, **425**, 130630.
- 30 H. Kwak, D. Han, J. P. Son, J. S. Kim, J. Park, K.-W. Nam, H. Kim and Y. S. Jung, *Chem. Eng. J.*, 2022, **437**, 135413.
- 31 F. D. Han, Y. Z. Zhu, X. F. He, Y. F. Mo and C. S. Wang, *Adv. Energy Mater.*, 2016, **6**, 1501590.
- 32 M. M. Thackeray and K. Amine, *Nat. Energy*, 2021, **6**, 566.
- 33 M.-J. Lee, S. Lee, P. Oh, Y. Kim and J. Cho, *Nano Lett.*, 2014, **14**, 993–999.
- 34 C. Wang, R. Yu, H. Duan, Q. Lu, Q. Li, K. R. Adair, D. Bao, Y. Liu, R. Yang, J. Wang, S. Zhao, H. Huang and X. Sun, *ACS Energy Lett.*, 2022, **7**, 410–416.